Journal of Zhejiang University-SCIENCE A (Applied Physics & Engineering) 2025 26(8):723-737
www.jzus.zju.edu.cn; www.springer.com/journal/11582
E-mail: jzus_a@zju.edu.cn

Research Article

https://doi.org/10.1631/jzus.A2400396

An energy-saving design method for additively manufactured integrated valve-controlled cylinders

Yang TANG[1*], Dengting LI[1*], Honghao LIU[1], Chao ZHANG[1], Wujun WANG[2], Jie CAI[3], Huayong YANG[1], Yi ZHU[1,4]✉

[1]*State Key Laboratory of Fluid Power and Mechatronic Systems, Zhejiang University, Hangzhou 310058, China*
[2]*Department of Energy Technology, KTH Royal Institute of Technology, Stockholm 10044, Sweden*
[3]*China Railway Construction Heavy Industry Corporation Limited, Changsha 410023, China*
[4]*Ningbo Global Innovation Center, Zhejiang University, Ningbo 315100, China*

Abstract: The integrated valve-controlled cylinder combines various control and execution components in hydraulic transmission systems. Its precise control and rapid response characteristics make it widely used in mobile equipment for aerospace, robotics, and other engineering applications. Additive manufacturing provides high design freedom which can further enhance the power density of integrated valve-controlled cylinders. However, there is a lack of effective design methods to guide the additive manufacturing of valve-controlled cylinders for more efficient hydraulic energy transmission. This study accordingly introduces an energy-saving design method based on additive manufacturing for integrated valve-controlled cylinders. The method consists of two main parts: (1) redesigning the manifold block to eliminate leakage points and reduce energy losses through integrated design of the valve, cylinder, and piping; (2) establishing a pressure loss model to achieve energy savings through optimized flow channel design for bends with different parameters. Compared to traditional valve-controlled cylinders, the integrated valve-controlled cylinder developed from our method reduces the weight by 31%, volume by 55%, and pressure loss in the main flow channel by over 30%. This indicates that the design achieves both lightweight construction and improved hydraulic transmission efficiency. This study provides theoretical guidance for the design of lightweight and energy-efficient valve-controlled cylinders, and may aid the design of similar hydraulic machinery.

Key words: Valve-controlled cylinder; Additive manufacturing; Flow channel design; Energy-saving machinery; Integration

1 Introduction

The valve-controlled cylinder is a crucial power unit within hydraulic transmission systems, and is typically comprised of a motor, a pump, a controller, various control valves, and a hydraulic cylinder (Padovani et al., 2020). It enables local and independent movement, and finds application in aerospace, robotics, and other engineering machinery (Niraula et al., 2018; Zhang et al., 2018; Wu et al., 2020). Metal additive manufacturing technology currently holds significant potential for development in molding manufacturing methods (Huang et al., 2015; Pratheesh Kumar et al., 2021). This approach operates on the principle of piecewise superposition to create 3D objects with significant design flexibility (Satish Prakash et al., 2018), offering new possibilities for enhancing the performance, integration, and lightweight nature of valve-controlled cylinders.

For integrated valve-controlled cylinders with multiple components, additive manufacturing technology simplifies the original component layout. It reduces the number of connection joints and auxiliary process holes, and significantly decreases the weight of valve-controlled cylinders (Langelaar, 2018; Xie et al., 2020). It also eliminates sharp bends, resulting in improved flow channels (Pietropaoli et al., 2017; Zhang et al., 2020; McClain et al., 2021). Moog collaborated with an Italian research institute to develop an integrated valve-controlled cylinder that utilized additive manufacturing to integrate hydraulic cylinders, servo valves, sensors, and connecting channels. The cylinder achieved high-performance control while reducing energy loss and compacting the entire

✉ Yi ZHU, yiz@zju.edu.cn
* The two authors contributed equally to this work
Yi ZHU, https://orcid.org/0000-0003-0401-316X

Received Aug. 19, 2024; Revision accepted Dec. 3, 2024;
Crosschecked May 15, 2025; Online first July 18, 2025

actuator structure (Barasuol et al., 2018). Wang et al. (2022) redesigned a three-degree-of-freedom robot actuator with a rotating hydraulic cylinder using additive manufacturing technology, which increased the output torque of the actuator while reducing its weight and volume. Boston Dynamics used additive manufacturing to form an entire leg actuator, improving the hydraulic flow channel efficiency and enhancing the cooling capacity, and utilized multi-materials for increased functionality and durability of this part (Bhatti et al., 2015; Rezazadeh et al., 2018). Huang et al. (2021) employed additive manufacturing technology to develop lightweight designs for actuators, specifically utilizing topology optimization and carbon fiber composites to eliminate excess materials and reduce the overall weight of an actuator by more than 50%. In terms of flow channel optimization, Coletti et al. (2013) utilized segmented Bessel parameter curves to optimize the fabrication of U-shaped pipes through additive manufacturing, and achieved a 36% reduction in pressure loss. Similarly, Zhang et al. (2019) introduced a flow channel generation and connectivity rule, employing a layout method to construct 3D flow channel models. This approach resulted in a 74.6% decrease in pressure loss for typical internal flow channels and a 25.1% reduction in total volume. The actuator designs discussed above have served as important references for designing integrated valve-controlled cylinders. However, current research primarily focuses on designing component structures based on existing experience, without establishing scientific design criteria or processes for additive manufacturing of the cylinders.

Therefore, this study presents a design method for energy-saving integrated valve-controlled cylinders using additive manufacturing. Following the redesign and remanufacturing of a traditionally processed valve-controlled cylinder, the performance of the resulting cylinder is tested, with the goal of achieving lower weight and energy savings.

2 Prototype of the traditional valve-controlled cylinder

Fig. 1a depicts a conventional machined valve-controlled cylinder structure, featuring an electromagnetic directional valve, a hydraulic manifold block, and a combination of hydraulic cylinders. Its functionality relies on the integrated superposition of various functional components. These components operate independently, and the mechanical connections introduce numerous interfaces, thereby increasing the risk of leakage. Fig. 1b illustrates the hydraulic schematic of the valve-controlled cylinder system. Fluid is pumped from the tank by a motor-driven pump, passes through a filter and throttle valve, and is then controlled by an electromagnetic directional valve. This setup regulates the inflow and outflow of hydraulic oil to achieve the expansion and contraction of the piston rod within the cylinder. The relief valve vents high pressure. The material used for this valve control cylinder is 316L stainless steel; it weighs 10.37 kg with dimensions of 310 mm×97 mm×185 mm.

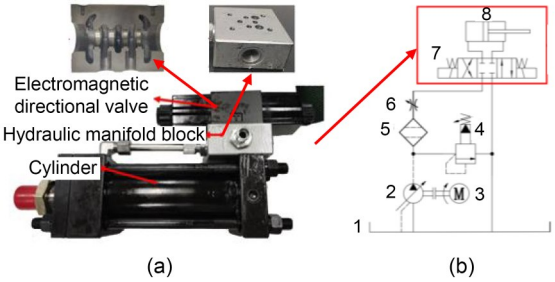

Fig. 1 (a) Conventional machined valve-controlled cylinder; (b) schematic of the hydraulic transmission system. 1: tank; 2: pump; 3: motor; 4: relief valve; 5: filter; 6: throttle valve; 7: electromagnetic directional valve; 8: hydraulic cylinder

3 Integrated structural design

Traditional valve-controlled cylinder structures rely on a stacked assembly of components, which can lead to a significant increase in system weight and volume, as well as a reduction in power density (Quan et al., 2014; Shang et al., 2018). Additive manufacturing enables the integration of multiple functional components into the hydraulic cylinder surface, facilitating energy savings and lightweight design through anisotropic structures that are challenging to construct using traditional processing methods. The overall structural design encompasses flow channel logic and integrated design of functional interfaces.

Fig. 2a illustrates the individual working oil holes in the original electromagnetic directional valve, while Fig. 2b depicts the individual working oil holes in the

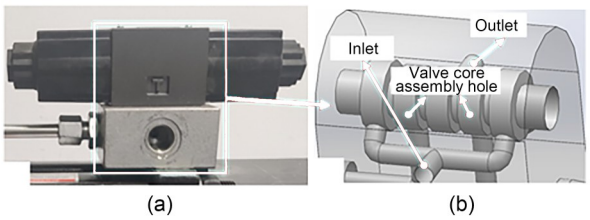

Fig. 2 (a) Integration of the traditional prototype valve body and manifold block; (b) integrated valve body and manifold block integration

integrated valve-controlled cylinder. When designing for integration, it is essential to ensure that one-to-one correspondence is maintained and the functionality unchanged after integration. Once the original functional interfaces are replicated, they should be connected based on their connection logic.

Utilizing the freedom of design offered by additive manufacturing, each interface is rearranged while ensuring the integrity of the original flow channel logic. In the layout design, Eq. (1) denotes the total number of assembly holes in the valve-controlled cylinder, and Eq. (2) represents the cumulative length of the flow channels:

$$N_{\min}=n_1+n_2+...+n_a, \tag{1}$$

$$L_{\min}=l_1+l_2+...+l_b, \tag{2}$$

where $N_{\min}$ is the minimum total number of assembly holes of the valve-controlled cylinder; n_j is the number of assembly holes in the valve-controlled cylinder (j=1, 2, ⋯, a); a is the number of connecting components; $L_{\min}$ is the cumulative length of the valve-controlled cylinder flow channel; l_i is the length of each flow channel (i=1, 2, ⋯, b); b is the total number of flow channels in the valve-controlled cylinder.

In this integrated design, our primary objective is to minimize the number of assembly holes and integrate each assembly interface directly with the flow channel or with other functional components. Simultaneously, we want to optimize the design for the shortest flow channel length and segment count. For instance, the design reduces local channels in the manifold block by directly integrating inlet and outlet holes, while a wall-mounted design is used to distribute flow channels both inside the manifold block and on the surface of the cylinder.

Table 1 illustrates the reduced height and weight of the valve-controlled cylinder, as well as the increased level of integration resulting from the use of an integrated design. This approach also minimizes the number of assembly holes for the valve-controlled cylinder, thereby reducing post-production machining requirements, streamlining assembly processes, enhancing system reliability, and mitigating the risk of hydraulic fluid leakage.

Table 1 Comparison between traditional manifold block integration and integrated manifold block integration

Parameter	Value	
	Traditional integration	Integrated integration
Height (mm)	120	70
Weight (kg)	1.94	1.16
Number of assembly holes in electromagnetic directional valve	10	2
Number of assembly holes in connecting flow channel	14	2

4 Integrated design of shared walls

When the flow channel is close to the cylinder surface in the integrated design, this shortens the length and reduces the volume of the valve-controlled cylinder. This also minimizes the support requirements during formation and subsequent machining processes. However, the use of shared walls can result in stress concentrations that cause reduced strength. In this study, ANSYS software was used to conduct stress modeling of the cylinder. A working pressure of 21 MPa was applied to both the valve-controlled cylinder and the internal flow channel. Displacement constraints were also imposed perpendicular to the unsealed end face to restrict movement in that direction. Fig. 3 depicts the stress distribution in the shared wall between a flow channel and a cylinder, with an inner diameter of 6 mm for the flow channel and 63 mm for the cylinder body. Compared to a single flow channel, there is an increase in maximum von Mises equivalent stress, particularly near the wall shared with the 6 mm flow channel.

Both the flow channel and the inner side of the cylinder are subjected to a uniform load of oil pressure. Upon the application of oil pressure, radial stresses and circumferential stresses are induced within the flow channel, causing both the flow channel and the cylinder to have a tendency to expand outward. However, at the junction between the flow channel and the cylinder, deformation in the radial direction is

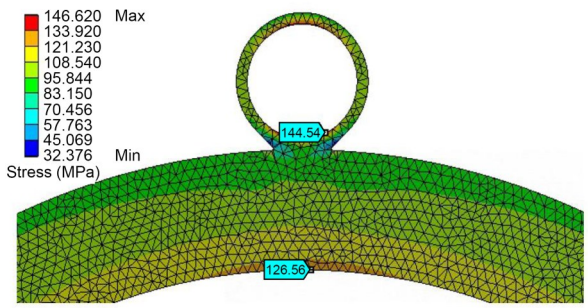

Fig. 3 Stress distribution in a shared wall

constrained, leading to increased deformation in the circumferential direction and a significant rise in circumferential stress at this location. Consequently, the point connecting the centers of the flow channel and the cylinder is where deformation is most restricted, resulting in the generation of maximum circumferential stresses. The integration between the flow channel and cylinder block connection leads to higher maximum stresses in the channels compared to those for a single channel.

By increasing the flow channel wall thickness and adjusting the diameter ratio of large-to-small flow channels, it is possible to reduce the stresses on the channels without altering the channel structure. Fig. 4 illustrates the maximum equivalent stresses σ_{eq} of the channel and cylinder at various diameter ratios, showing that stress levels effectively decrease as the diameter ratio increases.

Thus, when determining the distance for pressure-bearing components such as flow channels, it is essential to establish an appropriate distance that allows the

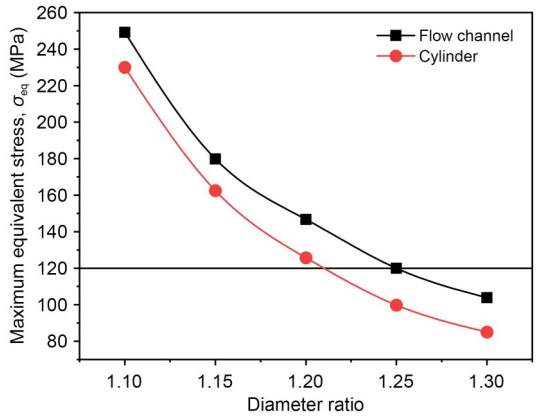

Fig. 4 Maximum equivalent stress of the flow channel and cylinder at various diameter ratios. The straight line y= 120 represents that the allowable stress for the flow channel and the valve-controlled cylinder is 120 MPa

component to deform freely under forces while not altering its original shape. For this type of pressure vessel channel, the stress magnitude is only considered under internal pressure conditions, as depicted in Eqs. (3)–(5):

$$\sigma_t = \frac{P}{(k^2-1)}\left(1+\frac{R_o^2}{r^2}\right), \tag{3}$$

$$\sigma_r = \frac{P}{(k^2-1)}\left(1-\frac{R_o^2}{r^2}\right), \tag{4}$$

$$\sigma_z = \frac{P}{k^2-1}, \tag{5}$$

where σ_t, σ_r, and σ_z represent the circumferential stress, radial stress, and axial stress borne by the flow channel, respectively; k is the ratio of the outer diameter to the inner diameter of the flow channel; P is the internal pressure borne by the flow channel; R_o is the outer diameter of the flow channel; r is the distance from a point in the channel wall to the center of the channel circle.

According to Hooke's law, the deformation condition of the circumferential flow channel under triaxial stress is:

$$e_t = \frac{1}{E}(\sigma_t - \mu\sigma_r - \mu\sigma_z), \tag{6}$$

where e_t is the circumferential strain of the flow channel under triaxial stress conditions; μ is Poisson's ratio of the material; E is Young's modulus of the material.

According to the deformation of the outer wall of the flow channel, we can obtain:

$$e_t = \frac{\Delta R}{R_o}. \tag{7}$$

Thus, the radial deformation ΔR of the flow channel is:

$$\Delta R = \frac{(2-\mu)PR_o}{E(k^2-1)}. \tag{8}$$

When using additive manufacturing technology to form channels, the influence of the laser spot diameter r_l can result in the formed entity being larger than the intended design size (Schmidt et al., 2017; Weaver et al., 2022). Therefore, when designing channel spacing, it is necessary to consider the impact of the

laser spot diameter. Assuming that the deformations in the radial direction of two neighboring parallel channels are ΔR_1 and ΔR_2, and that θ_h is the angle between a line connecting their centers and the horizontal line, then the designed gap d for the horizontally formed channels is:

$$d=\Delta R_1+\Delta R_2+\frac{r_1}{\cos\theta_h}. \tag{9}$$

The above formula is applicable for channels that share the same starting plane and are parallel to each other. When dealing with channels with overlapping angles or structures, printing parameters and the influence of support on channel formation must be considered in the spacing design.

5 Method for planning low-pressure loss channel paths

In valve-controlled cylinders, conventional flow channels are primarily shaped through drilling, milling, and other machining methods to achieve a change of direction with intersections mainly at right angles (Hagen et al., 2019; Xu et al., 2019). This type of transition not only leads to significant local pressure loss but also limits channel design. Additive manufacturing offers a high degree of design freedom, enabling new concepts for hydraulic unit channel design. The pressure loss in hydraulic channels typically consists of frictional pressure loss and local pressure loss. While there is an accurate model for calculating the frictional pressure loss in additive manufacturing flow channels (Zhou et al., 2021), there is a lack of models that can precisely predict local pressure loss.

5.1 Pressure loss model of bent channel

In this study, computational fluid dynamics (CFD) is employed to conduct the simulations of channels with varying bending ratios and angles under specific inlet conditions. The aim is to reveal the relationship between bending ratio, bending angle, and channel pressure loss in order to predict pressure loss in channels. Fig. 5 illustrates the simulated channel model. To ensure fully developed flow before the bent channel and to mimic realistic laminar flow conditions, a long straight flow channel precedes the bent flow channel, with measurement points placed at specific distances.

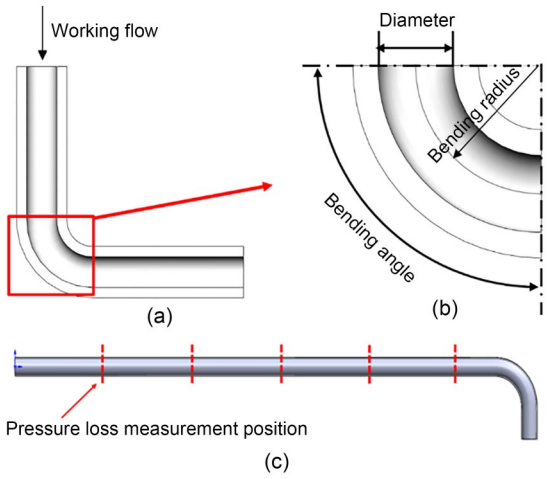

Fig. 5 Characteristic parameters of the bent channel. (a) Simulated channel model of the valve-controlled cylinder with varying bending ratios and inlet conditions; (b) pressure loss simulation in the bent flow channel under different flow rates and bending ratios; (c) relationship between bending ratio, bending angle, and pressure loss for the flow channel

The pressure loss at a bend is primarily attributed to two factors: frictional losses and losses caused by fluid separation during the turning process (Crawford et al., 2007). When the bending ratio of the flow channel—defined as the ratio of the channel bend radius to the channel radius—is small, the pressure loss in the curved section is predominantly due to fluid separation. On the contrary, when the bending ratio is relatively large, frictional losses become the main contributor to pressure loss.

For channels with high bending ratios under consistent inlet and boundary conditions, the pressure loss P_b can be estimated by Eq. (10) (Hashan Peiris et al., 2021):

$$P_b=pR\theta, \tag{10}$$

where R is the bending ratio of the flow channel; θ is the bending angle of the flow channel; p is the pressure loss per unit length at a specific bending angle, under stabilized conditions where fluid friction predominantly governs the pressure loss.

For flow channels with low bending ratios, however, accurate estimation formulas remain elusive. To address this gap, we conducted simulations and interpolation techniques to evaluate the pressure loss in channels with specified bending ratios. As a result, a correlation was established among the bending ratio,

bending angle, and flow channel pressure loss, providing a reliable method to predict pressure loss.

The working flow rates Q are set to 5, 15, 30, and 60 L/min, based on reference values for the valve-controlled cylinder. The simulation parameters are provided in Table 2. Based on the CFD simulation data points, the relationship is established using a bilinear interpolation function. Fig. 6 illustrates the pressure loss in the bent flow channel for varying operating flow rates, bending angles, and bending ratios. It is evident that as the bending ratio increases, the pressure loss of the channel initially decreases before rising again. This occurs because fluid separation is the primary cause of pressure loss in the bent channel at lower bending ratios; as the bending ratio increases, the fluid separation diminishes. At the same time, the elongated path of the bent channel causes an increase in wall friction-induced pressure loss. Once it surpasses a certain threshold, wall friction becomes the primary cause of pressure loss in the channel and exhibits a strong linear correlation with the bending ratio.

Table 2 Simulation calculation parameters

Parameter	Description
Feature length (mm)	6
Working medium	Hydraulic Oil, ISO VG 46, AW
Viscosity (Pa·s)	0.03956
Density (kg/m^3)	860
Temperature (°C)	40
Grid shape	Hexahedral mesh
Speed inlet boundary conditions (m/s)	8.84, 17.68, 26.52, 35.36
Pressure outlet boundary conditions (Pa)	0
Solving models	Renormalization group (RNG) based k–ε turbulence model
Residual convergence tolerance	10^{-6}
Number of iterations	1500

5.2 Mathematical model for the path design of low-pressure loss channel

The theoretical prediction of pressure loss for a channel in any given condition can be obtained using the aforementioned database. For example, Fig. 7 illustrates the hydraulic component formed by additive manufacturing and its flow channels. The flow channels of the valve-controlled cylinder can be divided into direct-current (DC) channels l_1, l_2, and l_3, as well as bent channels S_1, S_2, and S_3.

For an incompressible steady-flow fluid, the average velocity of the fluid remains constant when the inlet cross-sectional area is equal to the outlet cross-sectional area. In other words, it is necessary to

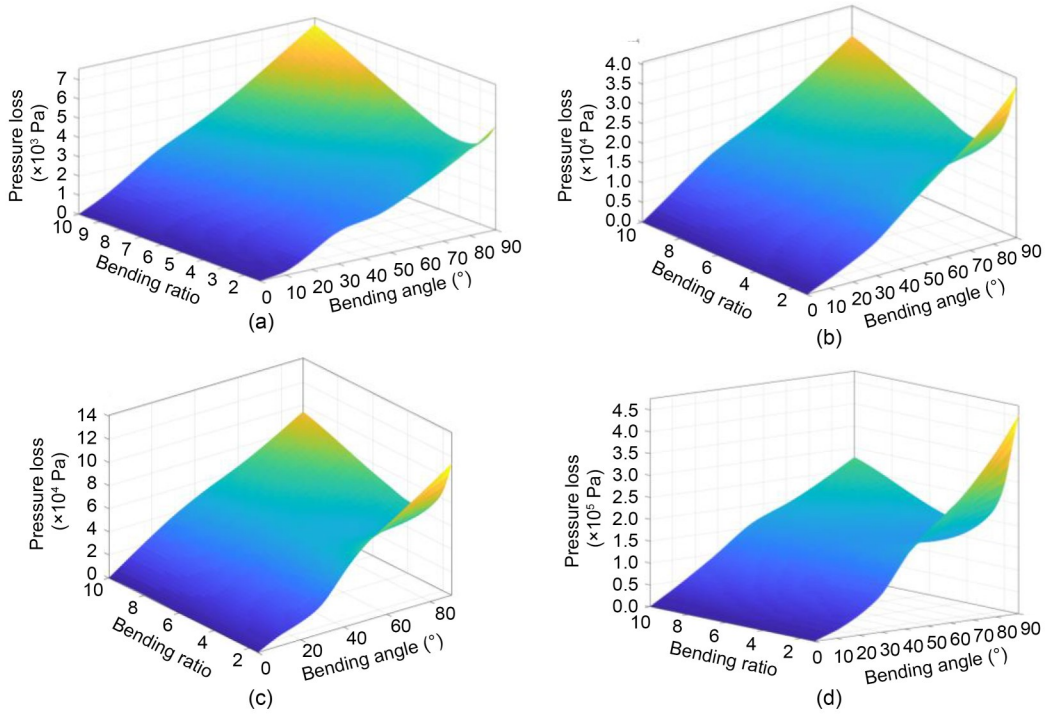

Fig. 6 Plots of bending angle, bending ratio, and pressure loss in the bent channel for operating flow rates of (a) 5 L/min, (b) 15 L/min, (c) 30 L/min, and (d) 60 L/min

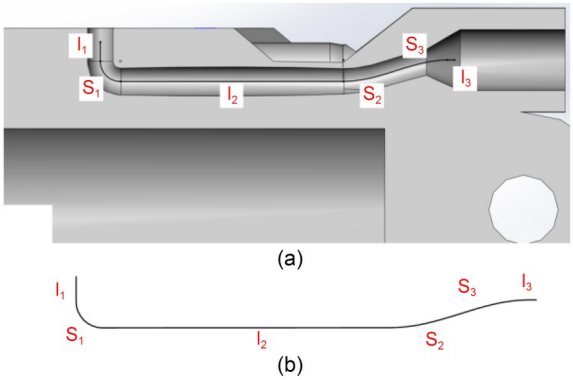

Fig. 7 (a) Additive manufacturing constructed valve-controlled cylinder; (b) channel path in the cylinder

calculate the average velocity at the inlet of each straight and bent channel to assess the operating flow rate for steady-state operation. Once the bending radius and bending angle of each corner channel are determined, pressure loss for that corner channel can be obtained by querying the database from a previous section. An evaluation function for assessing flow performance within a flow channel of the valve-controlled cylinder is established as shown:

$$P_{\min}(Q) = \sum \Delta P_s(Q, R, \theta) + \sum \Delta P_l(Q), \quad (11)$$

where $P_{\min}$ is the minimum pressure loss value for the function; $\sum \Delta P_s(Q, R, \theta)$ is the sum of the pressure loss values of the bent channels at the working flow rate Q, bending ratio R, and bending angle θ; $\sum \Delta P_l(Q)$ is the sum of pressure loss values of all DC channels at the working flow rate Q.

When designing hydraulic component channels, the known input condition typically involves the operating flow rate. Therefore, it is essential to establish the mathematical relationship between variations in channel shape, position, and other parameters of the bent and DC channels. This will enable us to predict the pressure loss across the channel. Fig. 8 illustrates the use of 3D coordinates for extracting parameters of the bent and DC channels, aiding the solution of the objective function.

For the bent channel, the parameters used to estimate its pressure loss include the starting spatial coordinate S_0, the bend point spatial coordinate S_1, and the endpoint spatial coordinate S_2. The bending angle θ is calculated using a vector composed of three points and can be obtained from Eq. (12):

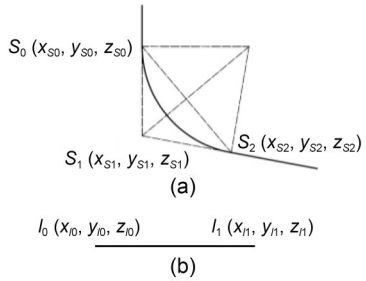

Fig. 8 (a) Bent channel parameters; (b) DC channel parameters

$$\theta = \arccos\left(\left|\frac{\overrightarrow{S_0S_1} \times \overrightarrow{S_1S_2}}{\left|\overrightarrow{S_0S_1}\right| \times \left|\overrightarrow{S_1S_2}\right|}\right|\right). \quad (12)$$

The bending ratio R can be calculated as:

$$R = \frac{R_s}{r} = \frac{\left|\overrightarrow{S_0S_2}\right|}{2 \times r \times \sin\left(\frac{\theta}{2}\right)}, \quad (13)$$

where R_s is the bending radius of the turning channel and r is the radius of the turning channel.

For the DC channel, knowing only the starting and ending coordinates is sufficient, and the length l can be obtained using Eq. (14) and then used to estimate its pressure loss.

$$l = \sqrt{(x_{l1} - x_{l0})^2 + (y_{l1} - y_{l0})^2 + (z_{l1} - z_{l0})^2}. \quad (14)$$

In designing the flow channel for the valve-controlled cylinder, it is essential to avoid interference with existing functional interfaces and necessary assembly space. Based on common component interface types and assembly space requirements for the valve-controlled cylinder, obstacles can be simplified into two categories: cylindrical (e.g., oil hole interfaces, cartridge valve interfaces, and their corresponding assembly spaces) and rectangular (e.g., plate valve assemblies).

5.3 Design of low-pressure loss flow channels for energy-saving valve-controlled cylinders

Including a bend in the channel of the cylinder helps to circumvent obstacles but also results in increased pressure loss. Therefore, optimizing the bend path design is crucial, as illustrated in Fig. 9.

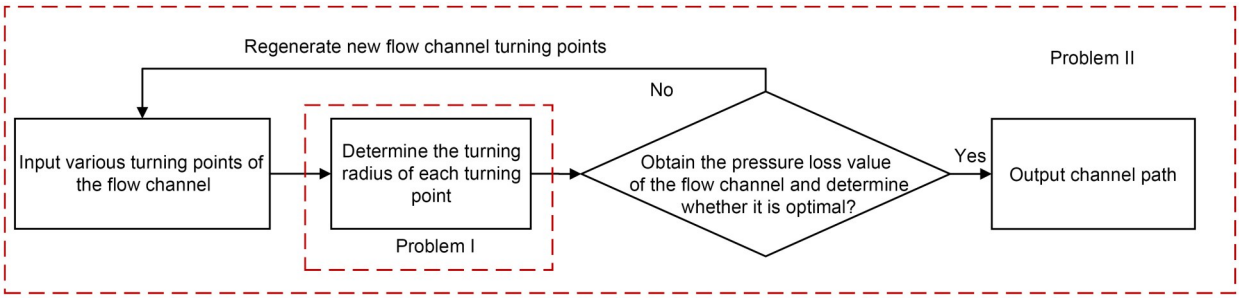

Fig. 9 Strategy for designing channels with minimal pressure loss

This solution process presents two primary challenges: (I) determining the optimal turning radius for each channel bend with predetermined locations; (II) comparing channels at different locations and identifying relatively optimal channels within global constraints.

The objective is to determine the turning radius of each segment within the flow channel along a given path. These turning radius values may be interdependent, as illustrated in Fig. 10a. For instance, the turning radius of channel S_1 can affect the range of possible values for the turning radius of channel S_2. Alternatively, these radii can be independent, as shown in Fig. 10b. Independence occurs when a "buffer channel" l_1 exists between turning channels S_1 and S_2, allowing their radii to vary independently. Therefore, solving this problem requires addressing multivariable coupling. To determine whether the two bent channels are mutually constrained or independent, the length of l_1 must be evaluated.

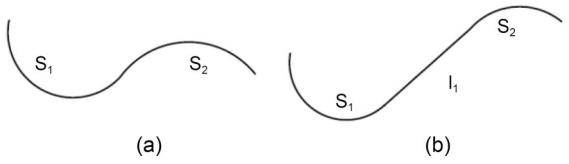

Fig. 10 (a) Two turning channels that are mutually constrained; (b) independent turning channels

Given that the number of bends in a single flow channel within a valve-controlled cylinder is relatively small, the optimization variables for minimizing pressure loss are limited to the turning radii of these bends. This constraint leads to a relatively small computational workload. Consequently, solving problem I could potentially involve enumerating across all possible configurations while ensuring that the iteration speed satisfies engineering requirements. Of course, the ultimate goal is to obtain the global optimal solution. Considering these factors, we selected the simulated annealing algorithm for solving problem I.

The simulated annealing algorithm was inspired by the annealing process of metals and involves two key components: an outer loop representing the annealing process and an inner loop based on the Metropolis algorithm. The outer loop begins by setting an initial temperature, which decreases proportionally according to a predefined cooling coefficient until a preset termination temperature is reached. This process determines the number of iterations and the overall computational time. The inner loop evaluates the changes in the system's internal energy at a given temperature. If the internal energy decreases compared to the previous state, the new state is accepted. However, if the internal energy does not decrease, acceptance is determined probabilistically using probability P_p. This probabilistic acceptance allows the algorithm to escape local optima, overcoming a key limitation of linear descent methods such as the Newton descent method. The probability P_p is governed by the Metropolis criterion, as shown in Eq. (15) (Wu et al., 2018):

$$P_p = \begin{cases} 1, & E_{n+1} < E_n, \\ e^{-\frac{E_{n+1}-E_n}{T}}, & E_{n+1} \geqslant E_n, \end{cases} \tag{15}$$

where E_n and E_{n+1} represent the energy (or objective function value) at the current state n and the candidate state n+1, respectively; T is the system temperature controlling the acceptance probability of worse solutions;

The simulated annealing algorithm process is illustrated in Fig. 11. In the context of algorithm design, the term "internal energy" corresponds to the pressure loss in each flow channel along a given path.

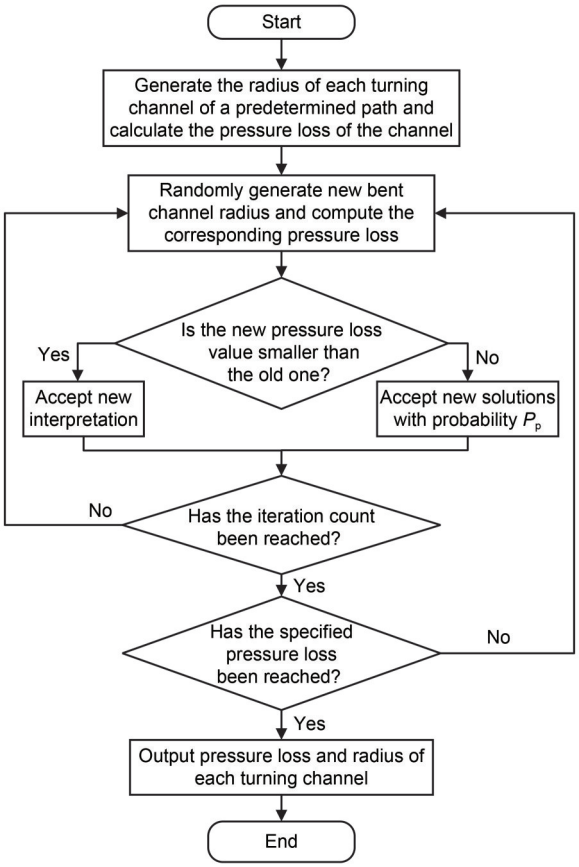

Fig. 11 Simulated annealing algorithm flowchart

As the temperature decreases during the simulated annealing process, the algorithm randomly generates a set of turning radii for each bent channel while satisfying the design constraints. During this stage, the algorithm ensures that the newly generated bent channels are effectively mutually constrained, avoiding any overlapping configurations.

Subsequently, different combinations of turning radii are compared, and the algorithm iteratively refines these configurations. The iteration process terminates when either the maximum number of iterations is reached, or the pressure loss converges to a stable value. Ultimately, this approach identifies the minimum pressure loss for the channel and determines the optimal turning radius for each bent channel, as shown in Fig. 11.

The objective of problem II is to determine the optimal flow path in 3D while satisfying the required design constraints. Achieving this requires evaluating each randomly generated flow path by solving problem I, wherein the turning radii and pressure losses are calculated. However, this process significantly increases the iteration time due to the need for repeated evaluations. Therefore, selecting an appropriate algorithm for problem II must consider factors such as the reliability of the algorithm's solutions, whether the error margin is acceptable for engineering standards, and computational efficiency. Considering these factors, the particle swarm optimization (PSO) algorithm, known for its strong global search capabilities and fast convergence, was chosen.

The PSO algorithm is inspired by the collective behavior of bird flocks, where each particle in the swarm represents a potential solution with attributes of velocity and position. Velocity reflects the particle's rate of movement, while position indicates its current direction. Each particle individually searches for the optimal solution within the search space, maintaining a record of its personal best solution p_{best}. Simultaneously, the algorithm evaluates all particles' solutions to determine the global best solution g_{best}. Subsequently, each particle adjusts its velocity and position based on both its personal optimal value and the global optimal value. The particle then begins the next iteration to search for the global optimal solution, as shown in Eqs. (16) and (17):

$$\boldsymbol{V}_i = w\boldsymbol{V}_i + mC_1(p_{\text{best},i} - \boldsymbol{X}_i) + mC_2(g_{\text{best},i} - \boldsymbol{X}_i), \quad (16)$$

$$\boldsymbol{X}_i = \boldsymbol{X}_i + \boldsymbol{V}_i, \quad (17)$$

where $\boldsymbol{V}_i$ is the velocity of the current particle; $\boldsymbol{X}_i$ is the position of the current particle; w is the inertia factor, which determines the influence of the particle's current state on its subsequent movement; m is the random number ranging from 0 to 1; C_1 and C_2 are the acceleration coefficients that control the balance between individual and global learning; $p_{\text{best},i}$ is the current personal best value for particle i; $g_{\text{best},i}$ is the global best value across all particles.

When applying PSO to problem II, the primary objective is to optimize the positions and angles of turning channels within the flow path. To achieve this, the algorithm focuses on the inflection points of the channels. Each particle is defined as a key inflection point in the turning channel, with its velocity and position extended into multiple dimensions to accommodate the 3D nature of the flow path. This multidimensional representation enables the algorithm to explore

a wide range of potential configurations, ensuring comprehensive optimization of the flow path.

The velocity and position of particles in the x, y, and z dimensions are updated using Eqs. (18) and (19). However, the concept of an "individual" in our algorithm needs to be more clearly defined; here, an "individual" does not refer to a single particle but rather to a complete flow channel. The individual optimal solution $p_{\text{best},i}$ corresponds to the minimum pressure loss value, obtained by solving problem I when the inflection point coordinates of each turning channel within the current flow channel are determined. At this stage, it is necessary to establish a 1D vector $\boldsymbol{p}_{\text{B},i}$, which contains the coordinates of each inflection point of the flow channel. This vector is used when the individual optimum solution is reached to update the iteration speed and spatial position of the inflection points, as shown in Eq. (20):

$$\boldsymbol{V}_i=[V_{ix},\ V_{iy},\ V_{iz}], \tag{18}$$

$$\boldsymbol{X}_i=[X_{ix},\ X_{iy},\ X_{iz}], \tag{19}$$

$$\boldsymbol{p}_{\text{B},i}=(P_{i1},\ P_{i2},\ \cdots,\ P_{ij}), \tag{20}$$

where i is the ith channel; j is the inflection point of the jth turning channel; P_{ij} is the coordinates of the jth inflection point on the ith channel.

The global optimal solution $g_{\text{best},i}$ corresponds to the minimum pressure loss value, across all flow channels. At this stage, it is also necessary to establish a 1D vector $\boldsymbol{g}_{\text{B}}$, which contains the coordinates of the inflection points for each turning channel when the global optimum is achieved. This vector is used to update the iteration speed and spatial position of the inflection points, as shown in Eq. (21):

$$\boldsymbol{g}_{\text{B}}=(G_1,\ G_2,\ G_3,\ \cdots,\ G_k), \tag{21}$$

where G_k is the coordinate of the kth inflection point on the channel.

Therefore, when updating the speed and position of the inflection points, the coordinates corresponding to both the individual optimal solution and the global optimal solution are updated in the x, y, and z dimensions, as shown in Eqs. (22) and (23):

$$V_{ij,x}=wV_{ij,x}+mC_1(P_{ij,x}-X_{ij,x})+mC_2(G_{k,x}-X_{ij,x}), \tag{22}$$

$$X_{ij,x}=X_{ij,x}+V_{ij,x}, \tag{23}$$

where the subscript 'ij,x' refers to the x-component (or coordinate) of the jth inflection point of the ith channel.

Therefore, compared to Eqs. (16) and (17), this equation has been expanded to include additional dimensions. Similarly, the same operation is applied to the y and z coordinates of each inflection point, increasing the dimensionality. After each update, it is necessary to determine whether the current global optimal solution g_{best} has been reached, or whether the algorithm has reached the maximum number of iterations. If neither condition is met, then the update process continues in a loop. If the conditions are met, then the final global optimal solution g_{best} and the coordinates $\boldsymbol{g}_{\text{B}}$ of each inflection point in the channel are output.

The global optimal solution represents the predicted minimum pressure loss value for the flow channel. By connecting the coordinates $\boldsymbol{g}_{\text{B}}$ of each inflection point with the inlet and outlet of the flow channel, the flow path is completed. Subsequently, using the turning radius of each turning channel, the input for each turning in the channel is determined, which yields the final channel path and completes the flow channel design. A flowchart of the PSO workflow we used is shown in Fig. 12.

The overall algorithm for our workflow is illustrated in Fig. 13. This algorithm involves setting the operating conditions of the channel and the entrance/exit locations. It also includes defining the design space of the valve-controlled cylinder based on preliminary design results, establishing the channel's design domain according to constraints, and characterizing and evaluating pressure loss using an objective function for fluid flow in valve-controlled cylinder channels. Additionally, spatial paths for channels are randomly generated using a particle swarm algorithm given the entrance and exit points. This approach utilizes a particle swarm algorithm to randomly generate a series of channels in space for a specific valve-controlled cylinder path, while employing a simulated annealing algorithm to obtain objective function values for each path. Subsequently, optimal solutions for all channels are iteratively solved using the particle swarm algorithm, which reveals the optimal spatial locations and bend designs. Finally, convergence is assessed; if the process converges, the inflection points of various bends along with their radii are output to complete the design of the valve-controlled cylinder channels.

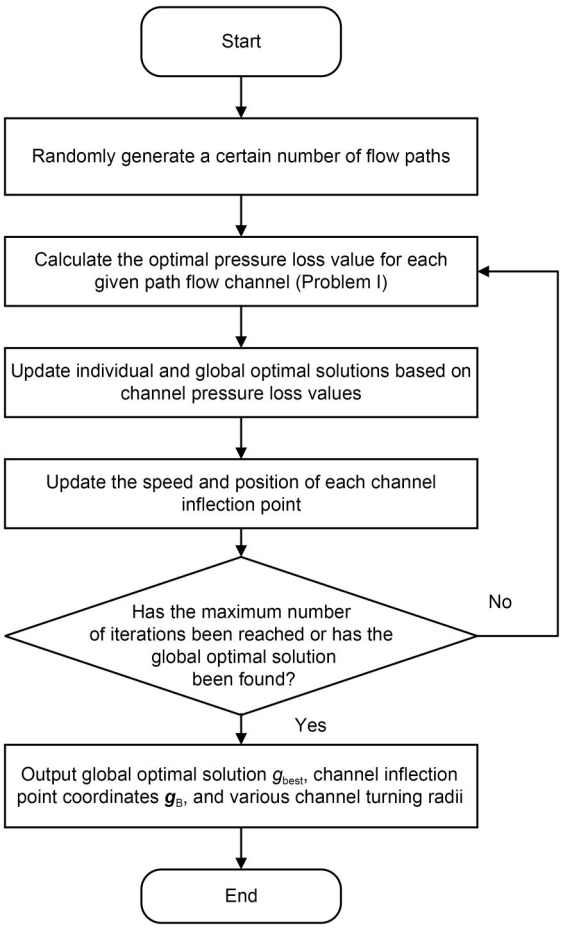

Fig. 12 Flowchart of PSO algorithm

5.4 Design of low-pressure loss flow channels for energy-saving valve-controlled cylinders

The results of applying the above algorithm to design the channel are shown in Fig. 14. The figure demonstrates that the algorithm prioritizes using a large turning radius and angle to minimize pressure loss along the channel while satisfying all constraints (He et al., 2021).

A CFD simulation was performed to validate the performances of these two flow channels. The simulation parameters are listed in Table 2, with a pressure of 21 MPa and a flow rate of 15 L/min. The measured pressure loss values were 53883 and 61458 Pa, while the predicted values were 47142 and 54921 Pa, resulting in errors of approximately 14.3% and 11.9%, respectively. These results demonstrate the accuracy of the algorithm in predicting pressure loss for both flow channels.

6 Additive manufacturing and testing of the energy-saving valve-controlled cylinder

Additive manufacturing technology is used for the formation of energy-saving valve-controlled cylinders, with process parameters detailed in Table 3. Given that the traditional prototype is made from

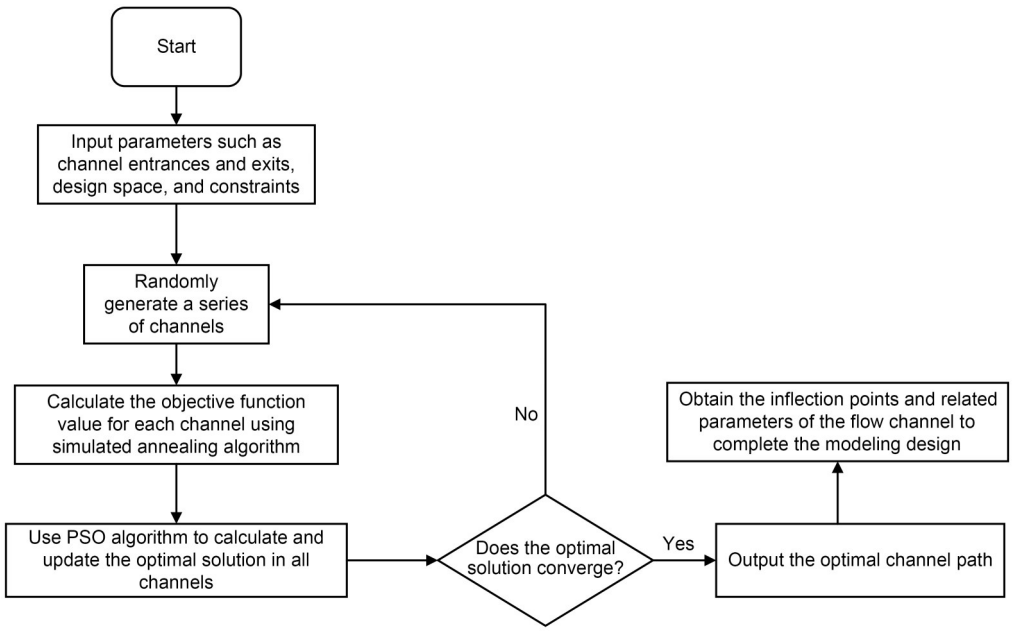

Fig. 13 Automated design solutions for minimizing pressure loss in hydraulic channels

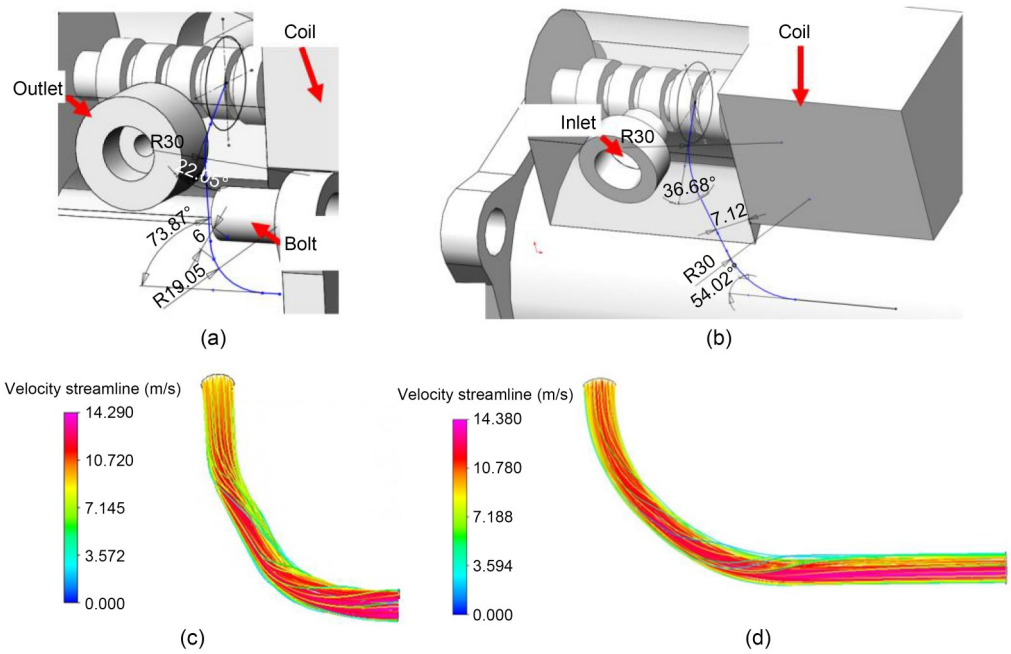

Fig. 14 (a and b) Automated design of manifold connections for the integrated valve-controlled cylinder (unit: mm); (c) simulation results for the flow channel between outlet and control hole; (d) simulation results for the flow channel between inlet and control hole

Table 3 Optimization of process parameters for additive manufacturing of the valve-controlled cylinder

Parameter	Description
Laser power (W)	200
Exposure time (μs)	80
Dot pitch (μm)	60
Scan spacing (μm)	110
Laser point diameter (μm)	70
Scanning strategy	Stripes

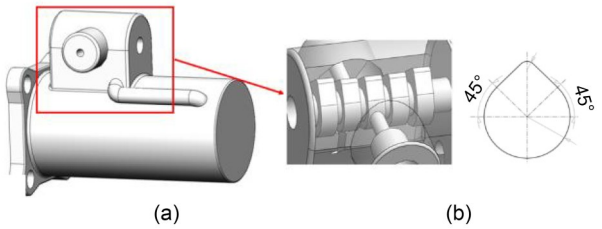

Fig. 15 (a) Structure of the directional valve spool; (b) support structure with a 'teardrop' shape

316L stainless steel, 316L stainless steel powder was selected as the forming material based on the operational requirements of the cylinder. Due to the specific characteristics of additive manufacturing, incorporating support structures for certain overhanging features is essential to ensure smooth formation (He et al., 2021; Weaver et al., 2022). The careful addition of these support structures not only improves the quality of the cylinder but also reduces the workload for subsequent machining. As shown in Fig. 15, the spool's position is designed with a 'teardrop' shape to ensure proper formation. Additionally, the barrel on the cylinder body is an overhanging structure and thus requires a shaped channel to facilitate its formation (Zhou et al., 2021).

After additive manufacturing, the valve-controlled cylinder housing underwent shot peening to improve its surface finish. The cartridge holes and threads necessary for assembly were then machined. Following machining, the end caps, solenoid coils, and piston rods were assembled as shown in Fig. 16. Compared to the traditional prototype valve-controlled cylinder, the final mass of the integrated cylinder was 7.19 kg, and the maximum space envelope dimensions were reduced to 201.25 mm×97.12 mm×135.00 mm, resulting in a weight reduction of approximately 31% and a space volume reduction of about 55%.

An experimental setup was constructed, as shown in Fig. 17, to measure pressure loss in the flow channel. A turbine flowmeter was used to measure the flow rate in the hydraulic oil pipes, with a range of 3–20 L/min and an accuracy of 1%. Pressure sensors were employed to detect the oil pressure, with a range of 0–25 MPa and a testing accuracy of 0.075%. A

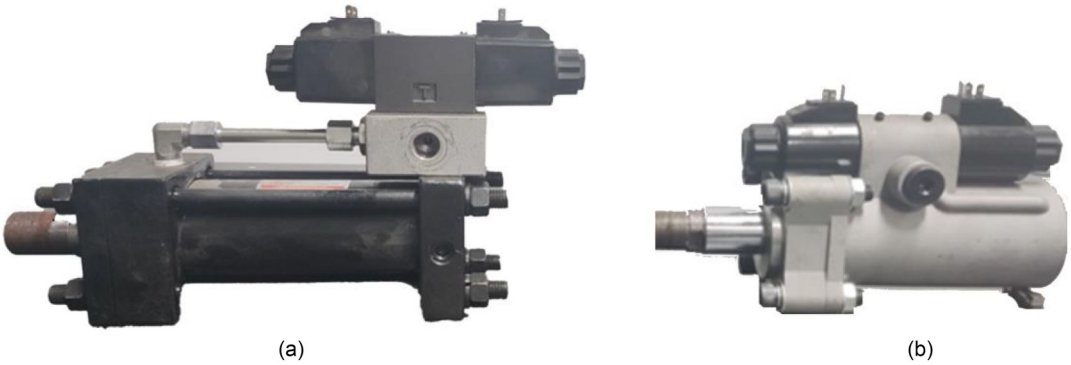

(a) (b)

Fig. 16 (a) Prototype of the traditional valve-controlled cylinder; (b) integrated valve-controlled cylinder

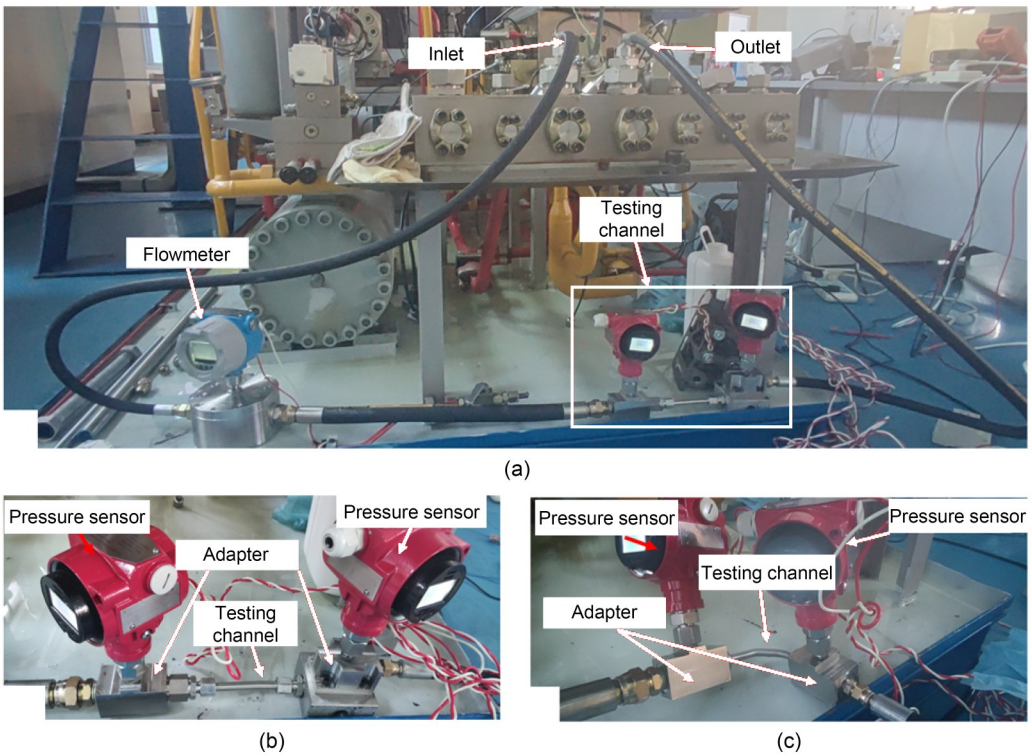

Fig. 17 (a) Experimental design for testing channel pressure loss; (b) traditional prototype channel testing; (c) integrated channel testing

three-phase adapter was used to connect the tested flow channel, pressure sensor, and oil pipe.

The experimental setup was configured with a pressure of 21 MPa, a working flow rate of 15 L/min, and No. 46 hydraulic oil as the working medium. The hydraulic oil temperature was set to 40 °C. The pressure loss was determined by reading the values from two pressure sensors and subtracting them to obtain the pressure difference. The final pressure loss result was calculated as the average of three test measurements, as shown in Table 4.

Table 4 Pressure loss test results

Channel type	Inlet pressure (MPa)	Outlet pressure (MPa)	Pressure loss (MPa)	Average pressure loss (MPa)
Traditional prototype	21.00	20.90	0.10	0.10
	21.01	20.90	0.11	0.10
	21.00	20.91	0.09	0.10
Integrated type	21.01	20.95	0.06	0.07
	21.01	20.92	0.09	0.07
	21.00	20.94	0.06	0.07

The results of the weight, volume, and pressure loss tests are shown in Fig. 18. The integrated valve-controlled cylinder channel significantly reduces pressure loss, showing a 30% improvement over the traditional prototype. However, the algorithm predicts an approximate 16% discrepancy between the simulated and actual experimental values for channel pressure loss, due to factors such as pipe friction not being modeled. Additionally, there is extra pressure loss at the connection point between the channel and the three-phase adapter during the test.

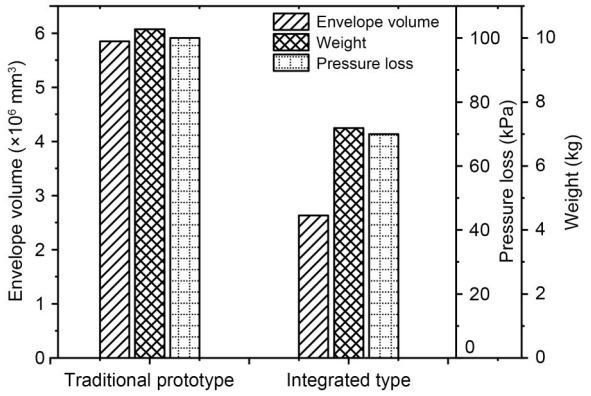

Fig. 18 Performance comparison between traditional prototype and integrated type valve-controlled cylinders

7 Conclusions

Additive manufacturing processes were used for energy-saving design and integrated molding of valve-controlled cylinders, which were previously machined using conventional methods. Flow performance tests were conducted to evaluate the final integrated valve-controlled cylinder, which was found to have significantly lower weight and volume while also having enhanced flow performance.

We demonstrated that an additive manufacturing approach successfully replicated the traditional prototype's hydraulic principles and allowed for the redesign of valve-controlled cylinder components, eliminating the need for hydraulic valve quick-connects and joints. Moreover, a design guideline for shared wall integration was proposed to minimize the need for print supports and prevent stress concentrations by reducing the distance between the channel and the cylinder. A pressure loss database was also created for channel bends at various operating flow rates, bending angles, and bending ratios. Based on this database, an automated design process for pressure loss-optimized flow channels in valve-controlled cylinders was developed.

Compared to the traditional prototype, the integrated valve-controlled cylinder was reduced by 31%, its volume was 55% lower, and its pressure loss was decreased by over 30%, all while improving flow performance. Based on the results of this study, our proposed design method bolsters the additive manufacturing of valve-controlled cylinders, and may also help with hydraulic valve manifolds and other components with similar structural and connective characteristics.

Acknowledgments

This work is supported by the National Natural Science Foundation of China (No. 52222503) and the Natural Science Foundation of Zhejiang Province (No. LD22E050003), China.

Author contributions

Yang TANG designed the research. Dengting LI and Honghao LIU processed the corresponding data. Yang TANG wrote the first draft of the manuscript. Chao ZHANG and Wujun WANG helped to organize the manuscript. Jie CAI and Huayong YANG revised and edited the final version. Yi ZHU supervised the study.

Conflict of interest

Huayong YANG is an Editor-in-Chief of this journal, and is NOT involved in the editorial review or the decision to publish this article. The authors declare that they have no conflict of interest.

References

Barasuol V, Villarreal-Magaña OA, Sangiah D, et al., 2018. Highly-integrated hydraulic smart actuators and smart manifolds for high-bandwidth force control. *Frontiers in Robotics and AI*, 5:51. https://doi.org/10.3389/frobt.2018.00051

Bhatti J, Plummer AR, Iravani P, et al., 2015. A survey of dynamic robot legged locomotion. International Conference on Fluid Power and Mechatronics, p.770-775. https://doi.org/10.1109/FPM.2015.7337218

Coletti F, Verstraete T, Bulle J, et al., 2013. Optimization of a U-bend for minimal pressure loss in internal cooling channels—part II: experimental validation. *Journal of Turbomachinery*, 135(3):051016. https://doi.org/10.1115/1.4023031

Crawford NM, Cunningham G, Spence SWT, 2007. An experimental investigation into the pressure drop for turbulent flow in 90° elbow bends. *Proceedings of the Institution of Mechanical Engineers, Part E: Journal of Process Mechanical Engineering*, 221(2):77-88. https://doi.org/10.1243/0954408JPME84

Hagen D, Padovani D, Choux M, 2019. A comparison study

of a novel self-contained electro-hydraulic cylinder versus a conventional valve-controlled actuator—part 1: motion control. *Actuators*, 8(4):79. https://doi.org/10.3390/act8040079

Hashan Peiris LD, Plummer A, Roesner J, et al., 2021. Prediction of flow path pressure drops in curved galleries for additively manufactured hydraulic manifolds. Symposium on Fluid Power and Motion Control, No. V001T01A021. https://doi.org/10.1115/FPMC2021-68676

He W, Deng QH, Yang GY, et al., 2021. Effects of turning angle and turning internal radius on channel impingement cooling for a novel internal cooling structure. *Journal of Turbomachinery*, 143(9):091005. https://doi.org/10.1115/1.4050608

Huang H, Zhang JH, Xu B, et al., 2021. Topology optimization design of a lightweight integrated manifold with low pressure loss in a hydraulic quadruped robot actuator. *Mechanical Sciences*, 12(1):249-257. https://doi.org/10.5194/ms-12-249-2021

Huang Y, Leu MC, Mazumder J, et al., 2015. Additive manufacturing: current state, future potential, gaps and needs, and recommendations. *Journal of Manufacturing Science and Engineering*, 137(1):014001. https://doi.org/10.1115/1.4028725

Langelaar M, 2018. Combined optimization of part topology, support structure layout and build orientation for additive manufacturing. *Structural and Multidisciplinary Optimization*, 57(5):1985-2004. https://doi.org/10.1007/s00158-017-1877-z

McClain ST, Hanson DR, Cinnamon E, et al., 2021. Flow in a simulated turbine blade cooling channel with spatially varying roughness caused by additive manufacturing orientation. *Journal of Turbomachinery*, 143(7):071013. https://doi.org/10.1115/1.4050389

Niraula A, Zhang SZ, Minav T, et al., 2018. Effect of zonal hydraulics on energy consumption and boom structure of a micro-excavator. *Energies*, 11(8):2088. https://doi.org/10.3390/en11082088

Padovani D, Rundo M, Altare G, 2020. The working hydraulics of valve-controlled mobile machines: classification and review. *Journal of Dynamic Systems, Measurement, and Control*, 142(7):070801. https://doi.org/10.1115/1.4046334

Pietropaoli M, Ahlfeld R, Montomoli F, et al., 2017. Design for additive manufacturing: internal channel optimization. *Journal of Engineering for Gas Turbines and Power*, 139(10):102101. https://doi.org/10.1115/1.4036358

Pratheesh Kumar S, Elangovan S, Mohanraj R, et al., 2021. Review on the evolution and technology of state-of-the-art metal additive manufacturing processes. *Materials Today: Proceedings*, 46:7907-7920. https://doi.org/10.1016/j.matpr.2021.02.567

Quan ZY, Quan L, Zhang JM, 2014. Review of energy efficient direct pump controlled cylinder electro-hydraulic technology. *Renewable and Sustainable Energy Reviews*, 35:336-346. https://doi.org/10.1016/j.rser.2014.04.036

Rezazadeh S, Abate A, Hatton RL, et al., 2018. Robot leg design: a constructive framework. *IEEE Access*, 6:54369-54387. https://doi.org/10.1109/ACCESS.2018.2870291

Satish Prakash K, Nancharaih T, Subba Rao VV, 2018. Additive manufacturing techniques in manufacturing–an overview. *Materials Today: Proceedings*, 5(2):3873-3882. https://doi.org/10.1016/j.matpr.2017.11.642

Schmidt M, Merklein M, Bourell D, et al., 2017. Laser based additive manufacturing in industry and academia. *CIRP Annals*, 66(2):561-583. https://doi.org/10.1016/j.cirp.2017.05.011

Shang YX, Liu XC, Jiao ZX, et al., 2018. An integrated load sensing valve-controlled actuator based on power-by-wire for aircraft structural test. *Aerospace Science and Technology*, 77:117-128. https://doi.org/10.1016/j.ast.2018.02.030

Wang WJ, Tang F, Zheng C, et al., 2022. Prototyping a novel compact 3-DOF hydraulic robotic actuator via metallic additive manufacturing. *Virtual and Physical Prototyping*, 17(3):617-630. https://doi.org/10.1080/17452759.2022.2045693

Weaver JS, Heigel JC, Lane BM, 2022. Laser spot size and scaling laws for laser beam additive manufacturing. *Journal of Manufacturing Processes*, 73:26-39. https://doi.org/10.1016/j.jmapro.2021.10.053

Wu GH, Yang JH, Shang JZ, et al., 2020. A rotary fluid power converter for improving energy efficiency of hydraulic system with variable load. *Energy*, 195:116957. https://doi.org/10.1016/j.energy.2020.116957

Wu XD, Bai WB, Xie YE, et al., 2018. A hybrid algorithm of particle swarm optimization, metropolis criterion and RTS smoother for path planning of UAVs. *Applied Soft Computing*, 73:735-747. https://doi.org/10.1016/j.asoc.2018.09.011

Xie GL, Dong YJ, Zhou J, et al., 2020. Topology optimization design of hydraulic valve blocks for additive manufacturing. *Proceedings of the Institution of Mechanical Engineers, Part C: Journal of Mechanical Engineering Science*, 234(10):1899-1912. https://doi.org/10.1177/0954406220902166

Xu ZQ, Li WL, Liu XY, et al., 2019. Dynamic characteristics of coupling model of valve-controlled cylinder parallel accumulator. *Mechanics & Industry*, 20(3):306. https://doi.org/10.1051/meca/2019006

Zhang C, Wang S, Li J, et al., 2020. Additive manufacturing of products with functional fluid channels: a review. *Additive Manufacturing*, 36:101490. https://doi.org/10.1016/j.addma.2020.101490

Zhang H, Wang CY, Li CC, 2019. Optimization of flow channel in 3D printing hydraulic manifold block based on response surface method. The 8th IEEE International Conference on Fluid Power and Mechatronics, p.217-223. https://doi.org/10.1109/FPM45753.2019.9035793

Zhang JH, Chao Q, Xu B, 2018. Analysis of the cylinder block tilting inertia moment and its effect on the performance of high-speed electro-hydrostatic actuator pumps of aircraft. *Chinese Journal of Aeronautics*, 31(1):169-177. https://doi.org/10.1016/j.cja.2017.02.010

Zhou L, Zhu Y, Liu HH, et al., 2021. A comprehensive model to predict friction factors of fluid channels fabricated using laser powder bed fusion additive manufacturing. *Additive Manufacturing*, 47:102212. https://doi.org/10.1016/j.addma.2021.102212